JGR Space Physics

RESEARCH ARTICLE
10.1029/2023JA031529

Revised Magnetospheric Model Reveals Signatures of Field-Aligned Current Systems at Mercury

K. Pump[1], D. Heyner[1], D. Schmid[2], W. Exner[3], and Ferdinand Plaschke[1]

[1]Institute of Geophysics and Extraterrestrial Physics, Braunschweig, Germany, [2]Space Research Institute, Austrian Academy of Sciences, Graz, Austria, [3]European Space Agency, ESTEC, Noordwijk, The Netherlands

Key Points:

- We present a revised model of Mercury's magnetospheric magnetic field
- The model now includes an eastward ring shaped current and the neutral sheet current is calculated more precisely with Biot Savart's law
- The strength of the field-aligned currents increases with higher magnetic activity

Correspondence to:

K. Pump,
k.pump@tu-bs.de

Citation:

Pump, K., Heyner, D., Schmid, D., Exner, W., & Plaschke, F. (2024). Revised magnetospheric model reveals signatures of field-aligned current systems at Mercury. *Journal of Geophysical Research: Space Physics*, *129*, e2023JA031529. https://doi.org/10.1029/2023JA031529

Received 31 MAR 2023
Accepted 8 FEB 2024

Author Contributions:

Conceptualization: D. Heyner, Ferdinand Plaschke
Funding acquisition: D. Heyner
Investigation: K. Pump
Project administration: D. Heyner
Software: K. Pump
Supervision: D. Heyner, D. Schmid, Ferdinand Plaschke
Validation: K. Pump
Visualization: K. Pump
Writing – original draft: K. Pump
Writing – review & editing: D. Heyner, D. Schmid, W. Exner, Ferdinand Plaschke

Abstract Mercury is the smallest and innermost planet of our solar system and has a dipole-dominated internal magnetic field that is relatively weak, very axisymmetric and significantly offset toward north. Through the interaction with the solar wind, a magnetosphere is created. Compared to the magnetosphere of Earth, Mercury's magnetosphere is smaller and more dynamic. To understand the magnetospheric structures and processes we use in situ MESSENGER data to develop further a semi-empiric model of the magnetospheric magnetic field, which can explain the observations and help to improve the mission planning for the BepiColombo mission en-route to Mercury. We present this semi-empiric KTH22-model, a modular model to calculate the magnetic field inside the Hermean magnetosphere. Korth et al. (2015, https://doi.org/10.1002/2015JA021022, 2017, https://doi.org/10.1002/2017gl074699) published a model, which is the basis for the KTH22-model. In this new version, the representation of the neutral sheet current magnetic field is more realistic, because it is now based on observations rather than ad-hoc assumptions. Furthermore, a new module is added to depict the eastward ring shaped current magnetic field. These enhancements offer the possibility to improve the main field determination. In addition, analyzing the magnetic field residuals allows us to investigate the field-aligned currents and their possible dependencies on external drivers. We see increasing currents under more disturbed conditions inside the magnetosphere, but no clear dependence on the z-component of the interplanetary magnetic field nor on the magnetosheath plasma β.

1. Introduction

Mercury maintains a global but particularly weak, dynamo-generated offset dipole field (Anderson et al., 2012; Genova et al., 2021; Heyner et al., 2021) that is subject to an intense solar wind flow because of the planet's proximity to the Sun (Milillo et al., 2020). As a result, only a small magnetosphere forms in which the planet itself occupies a large volume fraction. Due to the small scale, the magnetosphere reconfigures swiftly to changing upstream solar wind parameters with a Dungey-cycle time of only about 2 min (Slavin et al., 2010) leading to a very dynamic magnetosphere. The solar wind particle density as well as the interplanetary magnetic field (IMF) change periodically on an annual time scale of 88 Earth days (James et al., 2017) due to Mercury's elliptic orbit around the Sun as well as on shorter time periods of solar wind variations.

The solar wind at Mercury typically exhibits a low plasma β (ratio of thermal to magnetic pressure) which facilitates magnetic reconnection at the day side magnetopause under low magnetic shear angles (Gershman et al., 2016; Poh et al., 2016; Sun et al., 2016) The solar wind drags reconnected flux tubes toward the night side and this process produces a shear layer beneath the magnetopause. This layer could be coincident with the boundary layer found by Anderson et al. (2011). From this shear layer so-called region 1 field-aligned currents (R1 FAC) may be generated (Johnson & Wing, 2015). The R1 FAC emerge at dawn and flow toward the dusk side. The planetary magnetic field guides these currents toward the planet and there these currents must be flowing to the dusk to form a closed circuit. Mercury is not able to sustain an atmosphere and thus it also lacks a persistent, thick ionosphere. Only a thin exo-ionosphere from planetary sodium ions (Milillo et al., 2020) may provide a current closure path (Pederson currents) above the planet (Exner et al., 2020). A large fraction of the FAC may also close via Ohmic currents through the planet itself despite the low conductivity of the crust and upper mantle (Anderson et al., 2014).

Previous studies have shown, that the R1 FAC system is quite persistent rather than occurring at special times as at Earth (Anderson et al., 2014). Mercury is thus tightly coupled to its environment. It is still an open question how the R1 FAC system reacts to changes in the solar wind. Hybrid simulations of the magnetosphere suggest that the

geometry of the R1 FAC system at Mercury strongly depends on the IMF direction (Exner, 2021). This remains to be verified using in situ orbital data.

Moreover there are several studies (Shi et al., 2022; Zhao et al., 2022) which identify a ring shaped current structure close to Mercury. Inconsistently, these descriptions differ as they describe a westward and an eastward flowing current with entirely different characteristics but there is general agreement that the detected structures are not an Earth-like.

So far, this data is provided by the MESSENGER (MErcury Surface, Space ENvironment, GEochemistry and Ranging) mission and its plasma instruments on-board. MESSENGER was the first probe to orbit Mercury (from 2011 to 2015) but only obtained close-in measurements from the northern hemisphere. The dual-spacecraft mission BepiColombo (Benkhoff et al., 2010, 2021), which will provide a global perspective, is en-route to Mercury and first orbital magnetic field measurements are expected in 2026 (Glassmeier et al., 2010; Heyner et al., 2021).

The aim of this study is to better understand the current systems around Mercury. In order to work out the signatures of the R1 FAC, we remove the average magnetospheric signal from the in situ data. For this, we update the semi-empirical magnetosphere model by Korth et al. (2015) by adapting the current systems especially on the night side. The residuals (data—model) are then projected onto the planetary surface. There, the curl gives the radial current density which is a proxy for the R1 FAC. We divide these current density maps by general magnetospheric activity, magnetic shear at the day side magnetopause (positive and negative $B_{\mathrm{IMF},z}$) as well as expected plasma β in the magnetosheath.

2. Model Concept

The KTH22-model (**K**orth-**T**syganenko-**H**eyner 20**22**) is a modular model of the magnetic field inside the Hermean magnetosphere. The model is based on a terrestrial model (Tsyganenko & Usmanov, 1982), which was adapted to Mercury by Korth et al. (2015) and improved by Korth et al. (2017). In this work, we present a further revised version of this model-type with further improved modules and model control parameters based on in situ data. The main differences to the previous works mentioned above are a slightly changed external field description as well as a data driven ansatz for the neutral sheet current and the eastward ring current. These will be described in more detail below.

For the description of the magnetic field at Mercury, two coordinate systems are relevant. The first one is the Mercury-Solar-Orbital (MSO) and the second one is the Mercury-Solar-Magnetic coordinate system (MSM). The vector basis for both of them is the same. The X-axis points toward the Sun, the Z-axis points toward north and the Y-axis completes the right-handed system pointing against the orbital motion of Mercury around the Sun. While the center of the MSO system coincides with the center of the planet, the center for the MSM system is located at the source point of the internal offset dipole moment, 479 km north of the planet's center (Anderson et al., 2012). For the following calculations, we use the magnetic field measurements of NASA's MESSENGER Mission which stayed in a highly elliptical orbit around Mercury from 2011 until 2015. We use 1-min-averaged data in the aberrated MSO-coordinate system assuming a constant solar wind velocity of 400 km/s. The KTH22 model input (coordinates at given location) and output (magnetic field at this location) are in MSO-coordinates. It should be mentioned that for the calculation of the magnetic field vector in the KTH22 model the coordinates are converted to the aberrated MSM-coordinate system. For each figure and each equation in this work the applicable coordinate system is given. Moreover we use a Disturbance Index (DI) which is taken from Anderson et al. (2013) to describe the general magnetospheric activity during each orbit.

2.1. Magnetopause Boundary

The solar wind is considered to be a perfectly diamagnetic medium, so the planetary field cannot penetrate into the solar wind in this approximation. Likewise, the IMF does not enter the magnetosphere. The boundary between the solar wind and the planetary field is the magnetopause. In this model, following Shue et al. (1997), the magnetopause boundary is prescribed as a rotational ellipsoid with a cylindrical approximation for the night side magnetopause in the MSM-system:

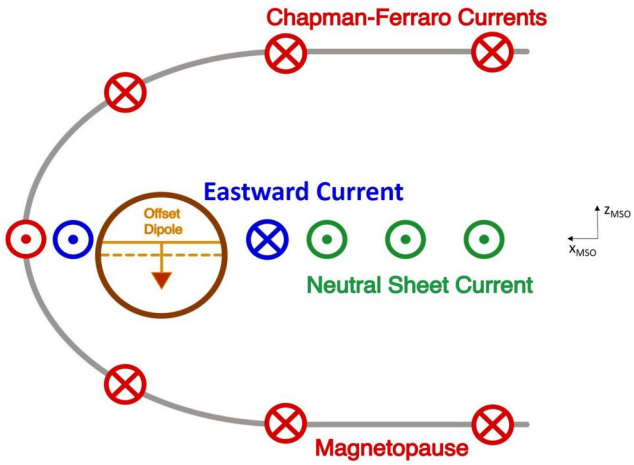

Figure 1. Sketch of the sources of the magnetic field in the KTH22 model in the noon-midnight meridional plane in the MSM-coordinate system (not to scale). The Sun is toward the left and the magnetosphere is bounded by the magnetopause (gray). Shielding currents (red) flow inside the magnetopause. The planet is shown in brown and the offset dipole moment (orange) points southward. On the night side, there are global current systems composed of the eastward ring shaped current (blue) and the neutral sheet current (green). These two current systems are anti-parallel to each other on the night side as indicated.

$$R_{MP} = R_{SS}\left(\frac{2}{1+\cos\varepsilon}\right)^{\alpha}. \quad (1)$$

Here, the subsolar magnetopause distance is R_{SS} with an average value of $1.42R_M$ (with $R_M = 2{,}440$ km being the planetary radius). The angle toward the x-axis is $\epsilon = \arctan\left(\frac{\rho_x}{x}\right)$ with $\rho_x = \sqrt{y^2+z^2}$ and the flaring constant is $\alpha = 0.5$ which leads to an asymptotic cylindrical shape of the magnetopause on the night side (Winslow et al., 2013). R_{MP} also depends on the heliocentric distance r_{hel} (distance between Mercury and Sun) and the DI and is implemented as in Korth et al. (2017). This DI ranges from 0 (quiet) to 100 (very disturbed) and is a measurement for the variance in the magnetic field in the magnetosphere for each orbit of the MESSENGER spacecraft (Anderson et al., 2013). The scaling parameters for the DI and r_{hel} are optimized by a fit to the data and can be found in Appendix A1. Inside the Hermean magnetosphere there are several processes and currents considered that generate a magnetic field:

- Offset dipole and higher multipoles produced by an internal dynamo process B_{dip},
- Neutral sheet current leading to B_{ns},
- Eastward ring shaped current leading to B_{rc}.

In this study, these magnetic fields are referred to as *internal* and are shown in Figure 1. In order to achieve the shielding at the magnetopause (via *Chapman-Ferraro Currents* in Figure 1), the magnetic flux normal to the magnetopause boundary is compensated by an external magnetic field B_{cf} derived from a scalar potential $\vec{B} = -\nabla\Psi_{cf}$. Thus, in principal, for every magnetic field source inside the magnetosphere there is a corresponding shielding field:

$$\vec{B} = \vec{B}_{dip} + \vec{B}_{rc} + \vec{B}_{ns} + \vec{B}_{cf,dip} + \vec{B}_{cf,rc} + \vec{B}_{cf,ns}. \quad (2)$$

Because of the rotational symmetry of the magnetopause, the scalar potential is expanded into cylindrical harmonics (Equation A4 in Appendix A2). In contrast to Korth et al. (2015), the center of the harmonics is not the planetary center but may vary along the x-axis between each cylindrical harmonic. This additional degree of freedom actually reduces the number of coefficients in the expansion necessary for a sufficient shielding at the magnetopause. The coefficients in this expansion (describing the geometrical structure of the shielding field) are found via a downhill simplex optimization (Nelder & Mead, 1965) procedure by minimizing the sum of the squared B_n components which is pointing into the normal direction of the magnetopause. The shielding fields include scaling factors which are determined from in situ data (see Appendix A1). The shielding between the magnetosphere and the magnetosheath is achieved in a least-squares sense.

2.2. Internal Dipole Field Model

Here, the internal field of Mercury is described as an axisymmetric dipole offset toward north in the MSM frame. The magnetic field of the offset dipole is described with a gradient of a scalar magnetic potential:

$$\vec{B}_{dip} = -\nabla\Psi_{dip}. \quad (3)$$

Thus, in a standard spherical coordinate system (r, θ, φ) with the origin at the location of the offset dipole, this magnetic field reads:

$$B_r = 2g^0_{1,int}\left(\frac{R_M}{r}\right)^3 \cos\theta \quad (4)$$

$$B_\theta = g^0_{1,\text{int}}\left(\frac{R_\text{M}}{r}\right)^3 \sin\theta \tag{5}$$

$$B_\varphi = 0. \tag{6}$$

Here, $g^0_{1,\text{int}}$ denotes the internal axial symmetric dipole coefficient. As offset toward the center of the planet, we use the value $d_\text{off} = 0.196\ R_\text{M} = 479$ km (Anderson et al., 2012). With the new updates of the model, we refit the internal dipole coefficient against all available in situ data from MESSENGER in the orbital phase. The method and outcome are presented in Section 2.5.

2.3. Neutral Sheet Current Model

Another important source of the magnetic field is the neutral sheet current. Korth et al. (2015) assume a quasi-Harris sheet for the modeling of the magnetic field of the neutral sheet current and use some ad-hoc assumptions to model the current density. This leads to an increasing neutral sheet current on the night side which converges to more than 800 nA/m^2 at far anti-sunward distances. In strong contrast to this, Rong et al. (2018) find a maximum current density of only about 80 nA/m^2 at a distance of ≈2.1 R_M of the planet on the night side based on MESSENGER magnetic field data.

The KTH22 module contains a revised version of the whole neutral sheet current module. By taking the Harris Sheet approach or using other transformation methods either the residuals on the day side or on the night side of Mercury showed huge deviations (>40 nT) from what can be seen in MESSENGER data, depending on the specific method how the parameters were obtained. To avoid this problem we instead use Biot Savart's law to directly calculate the magnetic field from a given current density profile. This leads to higher computing times but more realistic magnetic field calculations.

Therefore, we first improve the current density profile on the basis of findings from in situ magnetic field measurements rather than ad-hoc assumptions as in Korth et al. (2015). Assuming that the residuals are the magnetic fields from the remaining currents inside the magnetosphere, one can use the curl of this data to determine the current densities. To compute the current density $\vec{j}$ of the neutral sheet current from averaged magnetic field measurements $\vec{B}$, it is possible to use Ampères' law

$$\nabla \times \vec{B} = \mu_0\, \vec{j}. \tag{7}$$

We approximate the curl-operation by means of finite differences as in Rong et al. (2018). For this, the whole data set is divided into boxes with box sizes of 0.1 R_M in x- and z-directions and ±0.25 R_M in y-direction. For the calculation we use the median of the data taken per box. The y-component of the current density is approximated as

$$j_y = \frac{1}{\mu_0}\left(\frac{\Delta B_{x,\text{ns}}}{\Delta z} - \frac{\Delta B_{z,\text{ns}}}{\Delta x}\right), \tag{8}$$

where $B_{x,\text{ns}} = B_x - B_{x,\text{dipole}}$ and $B_{z,\text{ns}} = B_z - B_{z,\text{dipole}}$. Theoretically, the dipole magnetic field should have no influence on the curl operation, but here the subtraction is reasonable because the shielding field varies for different heliocentric distances and disturbance indices. The result is shown in the top plot in Figure 2. The current inside such a box is only calculated, when all four neighboring boxes contain at least one data point. At the edges of the area covered by MESSENGER (like on the far night side) some currents appear to be very strong, which has to be handled with caution. The reason therefore might be the choice of the box size. Inside those boxes there are sometimes just a few data points which were possibly measured under more extreme conditions. This leads to higher/lower values than average inside the box and thus to a stronger current. We suppose, that the neutral sheet current is the main contributor to the residuals (after subtracting the dipole field) on the night side further away from the planet than −1.3 R_M because this is the largest knwon stable structure on the night side.

From these results, a current density $\vec{j}$ for the neutral sheet current is calculated as

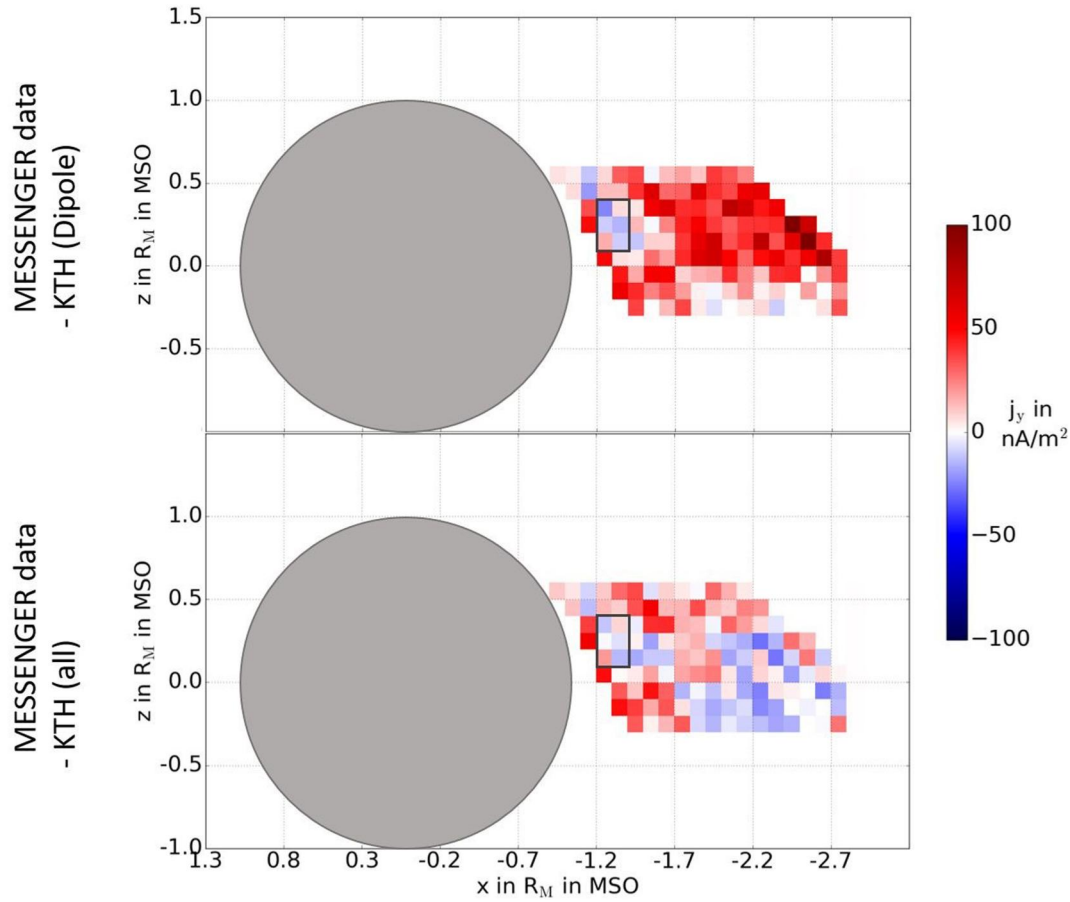

Figure 2. Both plots show the current in y-direction j_y in the *xz*-plane. For the top plot j_y is calculated from the curl of the magnetic field data of MESSENGER from which the dipole module (internal and corresponding cf-fields) of the KTH22 model has been subtracted. The bottom plot shows the current calculated from magnetic field data of MESSENGER from which all modules (dipole, neutral sheet current and eastward ring current with corresponding cf-fields) of the KTH22 model are subtracted. For these figures, the MESSENGER data within $|y| < 0.25\ R_M$ has been collected and the median was taken within each grid cell. Then, according to Equation 8 the curl was calculated on this gridded data. The black rectangle outlines the region of the eastward ring current on the night side.

$$\vec{j} = f_x \cdot f_y \cdot f_z \cdot \frac{\text{nA}}{\text{m}^2} \tag{9}$$

$$f_x = c_1(-x + c_2)^2 \cdot \exp\left(-c_3 \cdot (x + c_2)^2\right) \tag{10}$$

$$f_y = \exp\left(-c_4\, y^2\right) \tag{11}$$

$$f_z = \exp\left(-c_5\left(\frac{z}{c_6}\right)^2\right) \tag{12}$$

with x, y, z in R_M in the MSM-coordinate system, the parameters are $c_1 = 85\, R_M^2$, $c_2 = 1.0\ R_M$, $c_3 = 0.39\ \frac{1}{R_M^2}$, $c_4 = 0.5\ \frac{1}{R_M^2}$, $c_5 = 0.1$, and $c_6 = 0.12\ R_M$. The form of Equation 10 is a combination of a parabola and a Gaussian function which best describes the form of the neutral sheet current profile. The functions f_y and f_z limit the current sheet extend in the respective directions. All current density values inside the planet are set to zero. The parameters c_1–c_6 were obtained by least-squares fitting.

This profile is then implemented into the revised neutral sheet current module of the KTH22 model. With Biot Savart's law

$$\vec{B}_{\mathrm{ns}}\left(\vec{r}\right) = \frac{t \cdot \mu_0}{4\pi} \int_{V'} \frac{\vec{j}\left(\vec{r}\,'\right) \times \left(\vec{r} - \vec{r}\,'\right)}{\left|\vec{r} - \vec{r}\,'\right|^3} \mathrm{d}V' \tag{13}$$

the magnetic field can be computed at any point by integration over the neutral sheet current region. Here, $\vec{r} - \vec{r}\,'$ is the vector from the volume element $\mathrm{d}V'$ to the observation point $\vec{r}$.

Because the neutral sheet current only flows at the night side the integration volume V' can be reduced. Here, the bounds are set as $-5\,R_{\mathrm{M}} < x < -1\,R_{\mathrm{M}}$, $-1\,R_{\mathrm{M}} < y, z < 1\,R_{\mathrm{M}}$ using MSM-coordinates. The resulting magnetic field from Equation 13 is then multiplied by t, a disturbance index dependent scaling factor

$$t = t_a + \mathrm{DI} \cdot t_b \tag{14}$$

with $t_a = 0.725$ and $t_b = 0.0055$.

For the average value of the disturbance index (DI = 50), t equals 1. t_b is determined by fitting against in situ data and represents the increasing (decreasing) strength of the current under more (less) disturbed conditions. Therefore the MESSENGER data were divided into 5 parts with a DI-range of 20 ($0 < \mathrm{DI} < 20$, $20 < \mathrm{DI} < 40$, …, $80 < \mathrm{DI} < 100$). For each part the optimum factor t was found by least-squares fitting. The factor t is linearly dependant on DI as found by Korth et al. (2017). By strictly using standard numerical optimization with the whole set of MESSENGER data the smallest residuals between MESSENGER data and the KTH22 model are found for a higher factor t, so that the average $t(DI = 50) > 1$. The total residuum then decreases but the neutral sheet current is higher than what can be seen in the data. This means that there must be effects that are not yet implemented in the model and which are compensated by a too high magnetic field produced by the neutral sheet current.

2.4. Eastward Ring Current Model

In the residuals of the currents flowing in the y-direction in the top plot in Figure 2 one can discern a current close to the planet (marked with the gray square) pointing in the opposite direction ($-y$-direction, blue color) to the neutral sheet current. We identify this current as an eastward flowing ring current, which has also been depicted in other studies (Shi et al. (2022), visible in Figure 8 in Wang et al. (2022)). This current has different characteristics than the ring current we observe at Earth. Shi et al. (2022) call this current *eastward current* and find that it could be driven by a gradient in plasma pressure as a diamagnetic current, bounded at day side magnetopause. In contrast to this, Zhao et al. (2022) argue that there is a bifurcated westward-pointing ring current, which could be closed on the day side north and south of the magnetic equator. According to Zhao et al. (2022) this current is mainly driven by protons orbiting Mercury.

The studies mentioned above have in common that the authors observe ring-shaped structures close to the planet but they describe completely different characteristics. In summary there is no general agreement on the physics of a ring current at Mercury so far.

To address this issue we include a ring-shaped current structure in our model to analyze the characteristics. We first assume a rotationally symmetric current sheet at $z_{\mathrm{MSM}} = 0$ described by an azimutal vector potential

$$\vec{B} = t_{\mathrm{rc}} \nabla \times \vec{A} = t_{\mathrm{rc}} \nabla \times A_\varphi \vec{e}_\varphi \tag{15}$$

with $\vec{e}_\varphi$ being a unit vector in the azimutal direction and t_{rc} a scale factor obtained by fitting against MESSENGER data. Exploiting the rotational symmetry, the vector potential may be calculated as

$$A_\varphi = \int_0^\infty C(\lambda) J_1(\lambda\rho) \exp\left(-\lambda\sqrt{z^2 + d_0^2}\right) d\lambda \tag{16}$$

with $\rho = \sqrt{x^2 + y^2}$ where

$$C(\lambda) = \frac{\mu_0}{2} \int_0^\infty J_1(\lambda\xi) I(\xi) \xi d\xi. \tag{17}$$

A finite sheet thickness $d_0 = 0.16\ R_M$ is added in Equation 16 to obtain a 3D structure. C can be interpreted as a weight function (Tsyganenko, 1995). It contains all information of the ring shaped current profile I and is the so-called Hankel transform; μ_0 is the permeability of free space and J_1 is the Bessel function of the first kind. To describe this current profile I, a Gaussian function is chosen:

$$I = \frac{-0.4\ \text{kA}}{0.1\ R_M \sqrt{2\pi}} \cdot \exp - \frac{(\xi - 1.2\ R_M)^2}{2(0.1\ R_M)^2} \tag{18}$$

The numerical values included in Equation 18 are determined by minimizing the root-mean-square residuum

$$\Delta B = \sqrt{(B_{\text{KTH},x} - B_{\text{MES},x})^2 + (B_{\text{KTH},y} - B_{\text{MES},y})^2 + (B_{\text{KTH},z} - B_{\text{MES},z})^2}. \tag{19}$$

This minimization has been performed iteratively with the optimization of the dipole coefficient described in the following Section 2.5.

The bottom plot in Figure 2 shows the xz-plane of Mercury's magnetosphere in the same manner as the top plot but with subtraction of all KTH22-modules, including the revised neutral sheet current and the eastward ring current.

We can see that the residuals of the eastward ring current and the neutral sheet current between $0.0 < z < 0.5\ R_M$ are significantly reduced. This representation still shows a noisy background but the large-scale structures are represented in the model now. The average current density in the top plot of Figure 2 inside the outlined region is $j_y = -5.7\ \frac{\text{nA}}{\text{m}^2}$. After subtracting the KTH22 model magnetic field (including the eastward ring current) the average current density is $j_y = -0.51\ \frac{\text{nA}}{\text{m}^2}$ (bottom plot). The largest deviation on the night side is located between the eastward ring current and the planet (red). In this region there are only a few measurements of the magnetic field. On the other hand, there is also the possibility that these high currents are remnants of inaccuracies of the scaling (DI and r_{hel}) of the internal field. We conclude that an eastward flowing ring-shaped current module best explains the residuals in the MESSENGER data. The direction of the current in our results is in agreement with the findings of Shi et al. (2022). We do not modify the rotational symmetry of the eastward flowing current as described above. Therefore, the shape of the current does not match the shape found by Shi et al. (2022). The residuals are smallest when the eastward current is implemented as a closed current around the planet with the described parameters. On the night side the current is definitely visible. Due to the limitation of spatial coverage of magnetic field measurement there is only a slight indication that the current might close on the day side. Including a weaker magnetic field generated by the current on the day side leads to slightly worse residuals.

2.5. Adaptation of the Dipole Coefficient

An important parameter that was revised is the internal g_1^0 Gauss coefficient which describes the strength of the internal, axial dipole in a standard spherical harmonic expansion. In the post-MESSENGER literature, values ranging from −190 nT up to −223 nT can be found (Anderson et al., 2012; Wardinski et al., 2021). We estimate that $g_1^0 = -200.5$ nT gives the least residuals between the MESSENGER magnetic field measurements and the KTH22 model. To derive this parameter, all magnetic field measurements inside the Hermean magnetosphere from orbits with a disturbance index lower than 80 over the four Earth years of the MESSENGER mission are taken into account. The KTH22 model calculates an average state of the magnetosphere, so the most disturbed measurements are taken out. The internal dipole field, the revised neutral sheet current and the newly implemented eastward ring shaped current were determined iteratively with the shielding field at the magnetopause. For 5 different values of $g_{1\ \text{int}}^0$ the residuals are calculated by minimizing ΔB from Equation 19. ΔB is well described by a parabolic function:

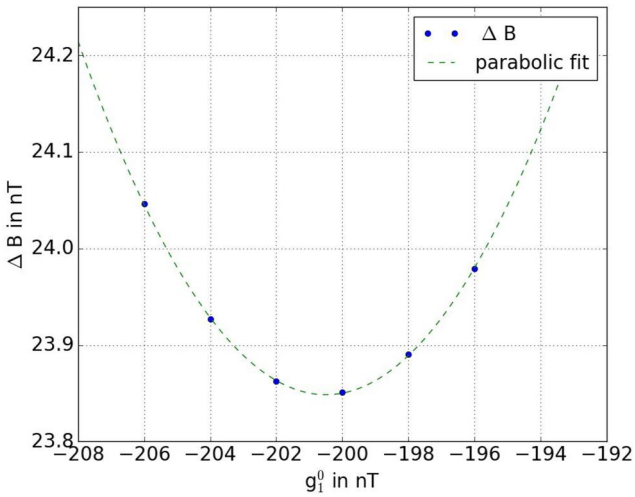

Figure 3. Average residuals between MESSENGER data and KTH22 model (ΔB) for different values of the internal g_1^0 coefficient.

$$\Delta B\left(g^0_{1\,\mathrm{int}}\right) = \frac{0.00651}{\mathrm{nT}} \cdot \left(g^0_{1\,\mathrm{int}}\right)^2 + 2.6097 \cdot g^0_{1\,\mathrm{int}} + 285.4726\,\mathrm{nT} \tag{20}$$

From these we determined an optimum at $g^0_{1\,\mathrm{int}} = -200.5\,\mathrm{nT} \pm 1.2\,\mathrm{nT}\,(3\sigma)$ with a total average difference between KTH22 model and MESSENGER data of 23.85 nT as seen in Figure 3.

3. Results

3.1. Results of the Improved Model

Figure 4 depicts field line traces which were determined with a Runge-Kutta-Algorithm of 4th order. Herewith the structure of the magnetosphere is well visible. In opposite to the fieldlines close to the day side magnetopause the ones on the far night side do not run parallel to the magnetopause anymore which means that the shielding at the day side is more decent than on the far night side (further away from the planet than 2 R_M). This is attributable to the fact that the optimization of the shielding parameters focused on the on the day side magnetopause because this region is covered by the MESSENGER spacecraft and is more of interest for further analysis. Furthermore there.

The collected MESSENGER-data, the improved model estimates and the differences between them are depicted in the x-z-plane in Figure 5. The bright area between $-1.5\,R_M < x_{MSO} < -2.5\,R_M$ in the ΔB_z-component indicates that the strength of the neutral sheet current matches the findings by MESSENGER.

Overall, structures in the residuals stemming from the neutral sheet current that are evident in the MESSENGER-data are significantly reduced. This means that the remaining residuals should mainly result from other sources than the internal dipole field, the neutral sheet current or the eastward flowing ring shaped current (see discussion in Section 4). With this revised model we investigate the residuals in the northern hemisphere, above the polar region. Figure 6 shows the residuals which we interpret as signatures of the field-aligned currents and the (Pedersen-like) closure currents.

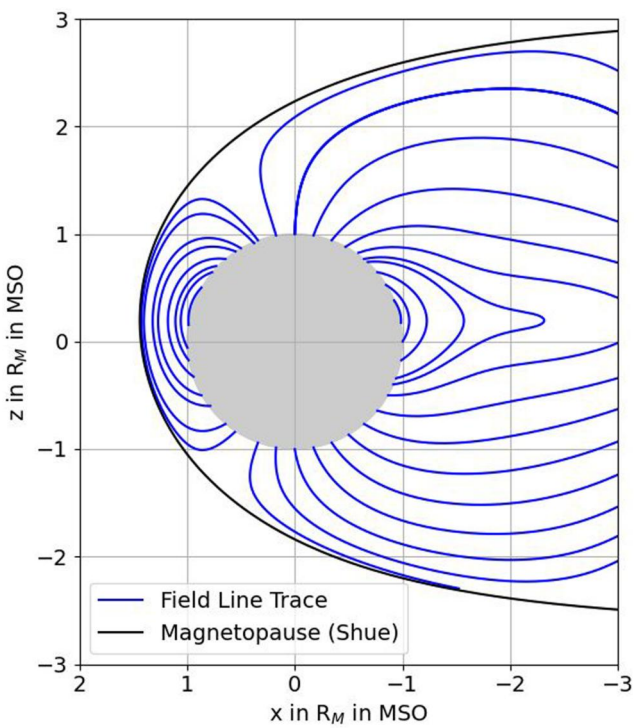

Figure 4. The blue lines show field line traces calculated from the KTH-Model which were computed with a Runge-Kutta-Algorithm of 4th order. The black line marks the Shue magnetopause.

3.2. Residual Analysis: Field-Aligned Current Signatures

Figure 6 shows the residuals in x-, y-, and z-direction projected in radial direction toward the center of the planet onto the northern planetary surface. Positive x-direction (MSO coordinates) points to the left (180°), toward the Sun. The magnetic field data measured in the northern hemisphere is taken, divided into subsets with sizes of 10° latitude and longitude and the average value per box is displayed in Figure 6. In this projection we can clearly see larger differences between the data and the model magnetic fields in the B_x- and B_z-component close to the poles.

The FACs are considered to flow from dawn to dusk, so in the pole region these currents and especially their closure currents lead to a higher B_x-component in the residuals, which decreases with increasing distance from the planet.

Due to the highly elliptical orbit of MESSENGER, the measurements taken above the north pole were taken at a lower distance to the planetary surface than the ones taken at regions closer to the equator, so the magnetic field strengths close to the pole are higher. To balance this overestimation of the FAC we introduce a leveling factor f_L

$$f_L = \frac{r}{R_M \cdot r_p} \tag{21}$$

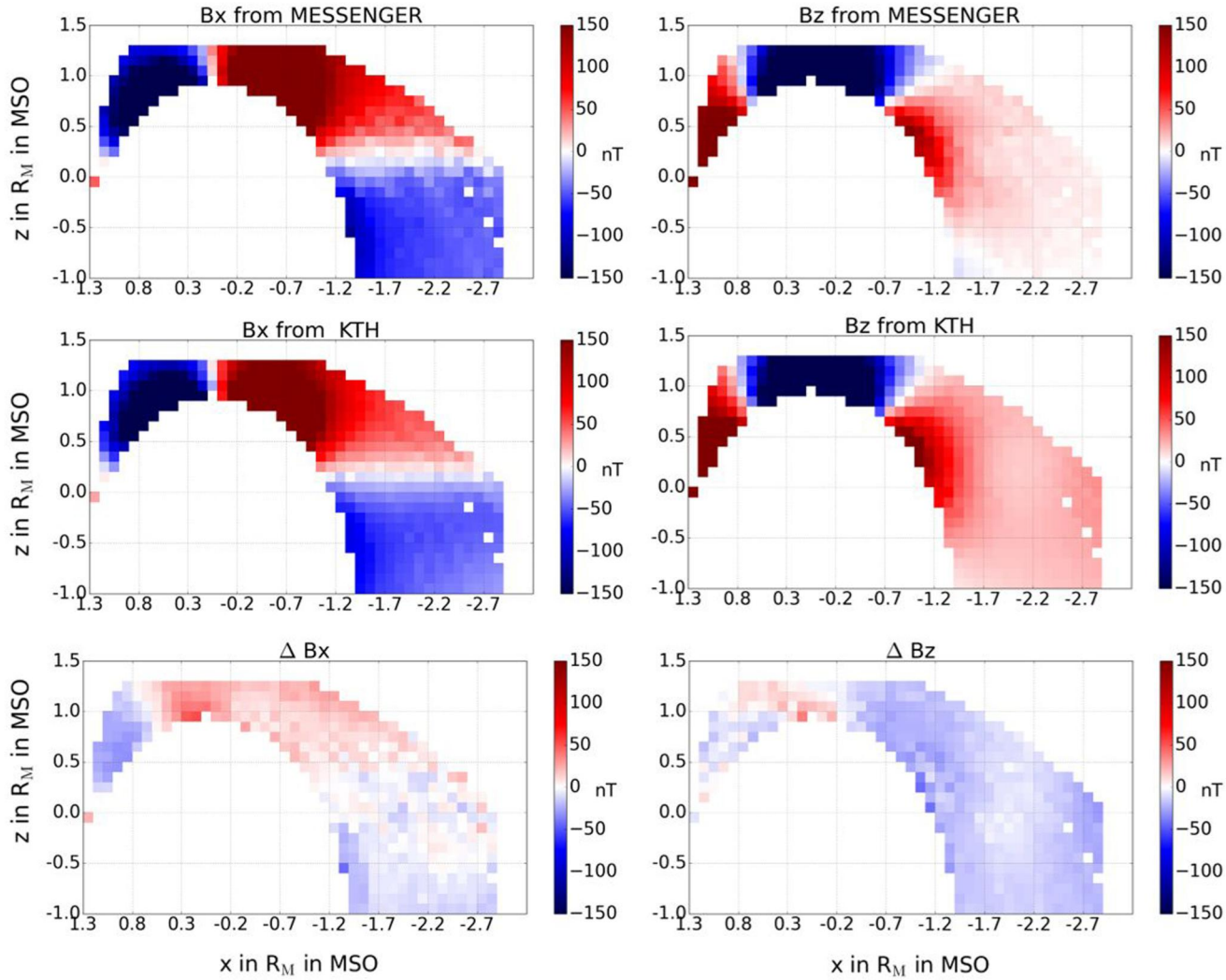

Figure 5. This figure shows the magnetic field data measured by MESSENGER in the top row, the magnetic field calculated with the KTH22 model in the middle and the difference between the measurement and the model in the bottom row. All values are the median within the boxes with box sizes x, $z = 0.1R_M$ and $|y| < 0.25R_M$.

where $r = \sqrt{x^2 + y^2 + z^2}$ is the radius (in MSO coordinates) of the location where the measurement of the magnetic field was taken and $R_M = 2{,}440$ km is the radius of Mercury. $r_p = 1.12\ R_M$ is the average distance to the planetary center at the pericenter of MESSENGER's orbit. This leveling factor is the reciprocal value of the factor one would use to project the elliptical shape of the orbit onto a spherical shell. According to Alexeev et al. (2000) we assume this $\frac{1}{r}$ decrease of the magnetic field of the FAC. To estimate the strength of the FAC the residuals are multiplied by the leveling factor (in spherical coordinates), then the curl operation is applied to yield the current in radial direction. We now analyze the radial currents, interpreted as R1 FACs. The current in radial direction j_r is calculated as

$$j_r = \frac{1}{\mu_0}\left(\frac{\Delta B_\varphi}{\Delta\theta} - \frac{\Delta B_\theta}{\Delta\varphi}\right), \tag{22}$$

with θ being the polar angle and φ being the azimuthal angle.

Anderson et al. (2013) found that there are steady state field-aligned currents present at Mercury. Investigating MESSENGER data they find only Region 1 currents which are about 100 times weaker than at Earth but also visible during magnetically quiet times.

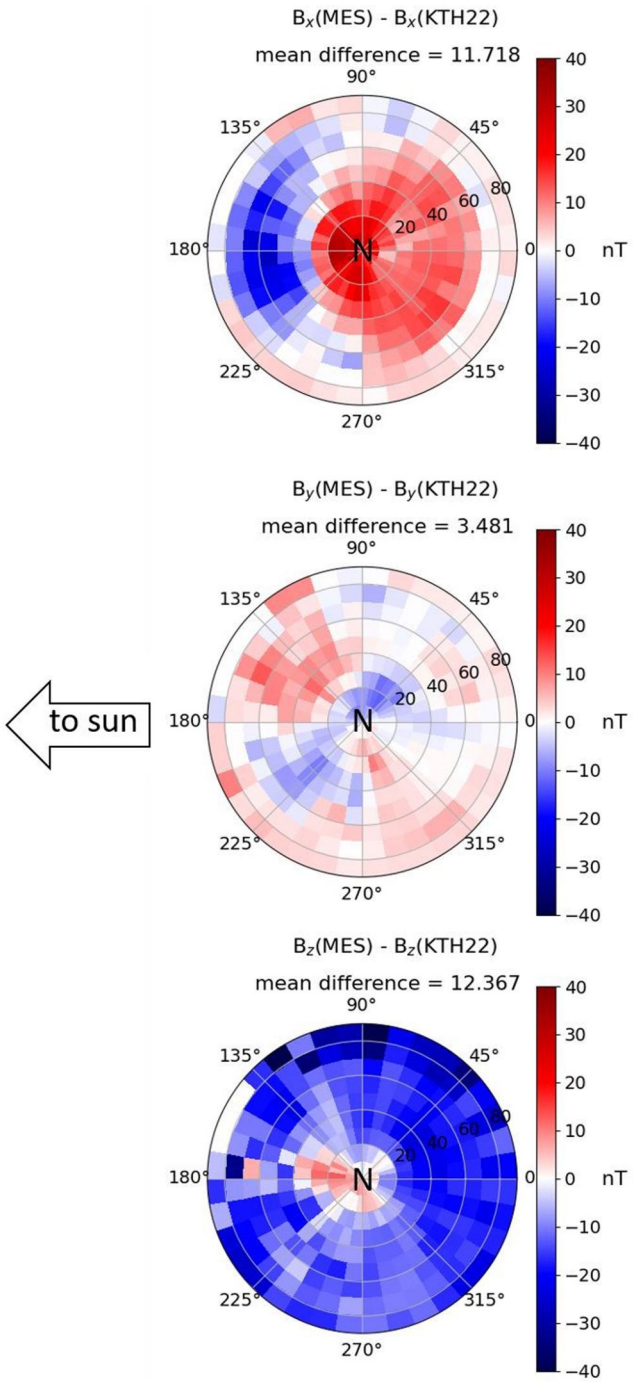

Figure 6. Residuals between MESSENGER data and KTH22 model field in x-, y-, and *z*-direction (top, middle, bottom) in MSO-coordinates.

In order to understand the driving mechanisms of the FAC, we investigate the form, strength and correlation with the DI, the direction of the IMF B_z-component and the plasma beta. A higher reconnection rate at the day side magnetopause leads to more magnetic flux normal to the magnetopause and thus to stronger field-aligned currents. This reconnection rate is controlled by the IMF shear angle θ and the plasma β of the magnetosheath (e.g., Johnson & Wing, 2015; Poh et al., 2016).

To analyze these dependencies we divide the data set into subsets, and calculate the radial current distributions for each of the subsets. The results are shown in Figure 7. The top row shows the currents calculated from magnetic field measurements at lower magnetic activity inside the magnetosphere (DI below 50, left) and under higher magnetic activity (DI above 50, right). The middle row shows a division into measurements from orbits with a negative (left) or positive (right) Bz-component of the IMF. Because there is no spacecraft monitoring the solar wind at the same time at Mercury, this division is an approximation from measurements taken in the solar wind before entering and after leaving the bow shock region. For simplicity, we assign a certain $B_{z,IMF}$ value to each MESSENGER orbit by linear interpolation between the IMF before and after bow shock crossing. Therefore, two 2-min time intervals of solar wind data are chosen that are separated from the inbound and outbound bow shock crossing by another 2 min, respectively. We interpolate it to the time of each pericenter crossing. Still, it has to be mentioned that this is just an estimation of the IMF direction. From James et al. (2017) we get a modal IMF magnitude of about $B = 20$ nT. The median time interval MESSENGER spent between the inbound and outbound bow-shock crossing is about 3 hr. The one-sided probability (forecast to future) of a sign-change in the IMF B_z for 1.5 hr is 70% according to James et al. (2017). Here, we interpolate between inbound and outbound bowshock crossings. Thus, we apply a two-sided interpolation (forecast to future and backcast to past). We estimate that the combined uncertainty for a 3 hr data gap in IMF knowledge is thus 49% at worst.

The bottom row shows a classification into measurements with high ($\beta > 0.7$) and low ($\beta < 0.7$) plasma-β in the magnetosheath. The value 0.7 is the median of the tao plamsa-β values and is chosen to divide the data into two subsets with approximately equal amounts of data. Note that there is no significant regime change between weak and strong reconnection at this value.

Due to the incomplete measurement coverage of plasma properties in the Hermean magnetosheath we combine plasma measurements from the FIPS instrument and TAO model to obtain plasma-β data. More details on the plasma-β estimation can be found in Section 3.3. Because both methods are just estimates, the classification into orbits with high and low plasma-β has been made in such a way that both the TAO and the FIPS (Andrews et al., 2007) estimation method have to result in the same categorization. This is the case for about 2/3 of the orbits. With the combination of both methods, the in situ measurement and the modeling, we gain a more reliable categorization. These values are preliminary estimates until more observations are available after BepiColombo has reached its orbit phase.

The black line in Figure 7 marks the open-closed-boundary (OCB). Inside of this line the magnetic field lines are denoted as *open*, outside (closer to the equator) they are *closed*. Here, field lines are *closed*, when both foot points begin/end on the surface of Mercury and the field line is not traced beyond $x = -2.5\ R_M$. For the field line tracing a 4th order Runge-Kutta-Algorithm is used with seed points evenly spaced (5°) in longitude and latitude directions.

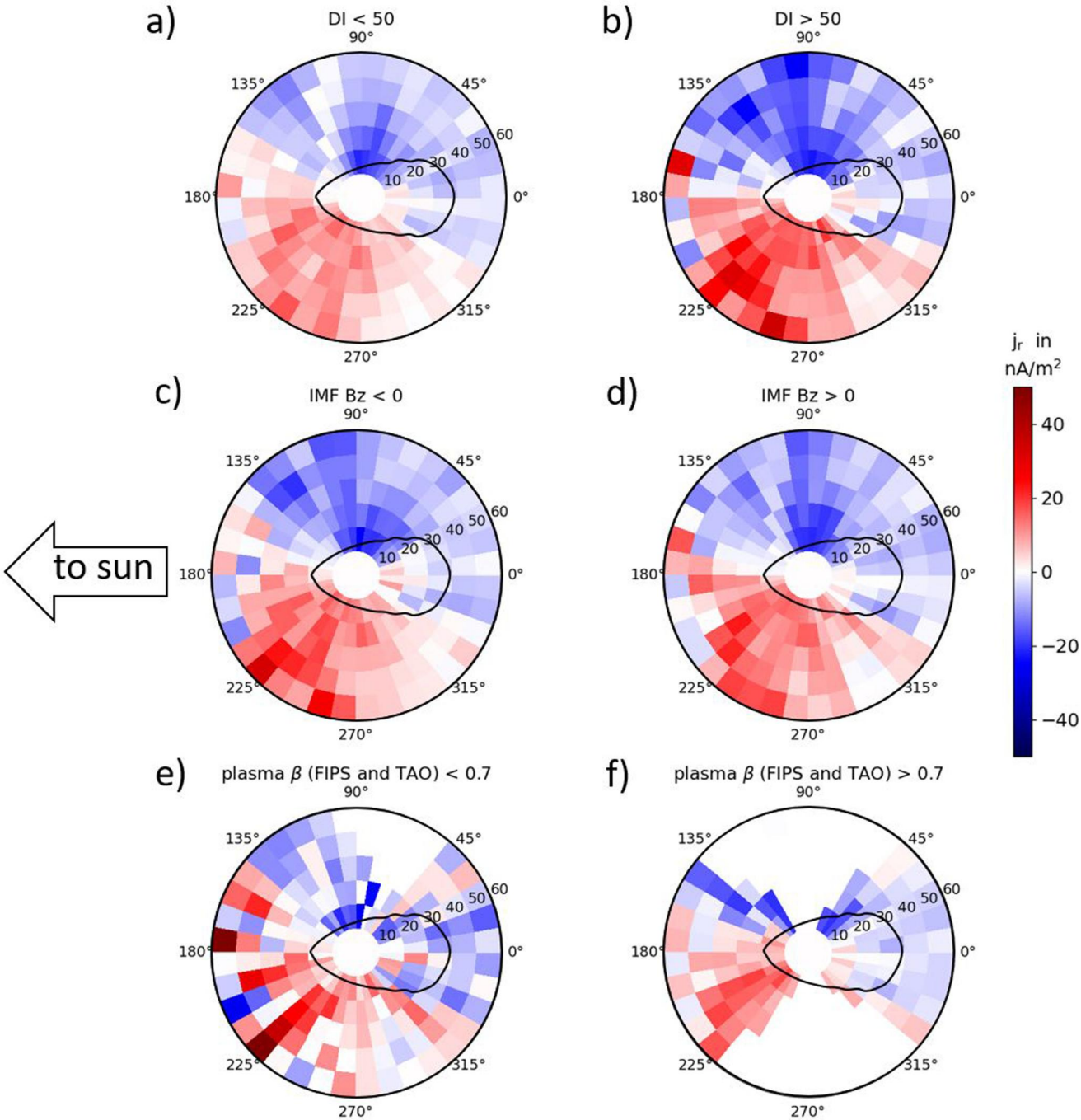

Figure 7. j_r (Field aligned currents) calculated from the curl of the residual magnetic field under different conditions, projected on the northern hemisphere. Top: low (a) and high (b) Disturbance Index. Middle row: negative (c) and positive (d) B_z-component of the IMF. Bottom row: low (e) and high (f) plasma β (lower/higher than 0.7) calculated with data from TAO model and FIPS instrument. The black oval marks the open-closed-boundary (OCB).

Anderson et al. (2014) find current densities of 10–30 nA/m^2. In this work we see slightly stronger field-aligned currents with densities of up to 40 nA/m^2 by analyzing the MESSENGER data.

3.3. Estimation of Plasma-β

In general, reconnection enhances the shear layer beneath the magnetopause. According to Johnson and Wing (2015), this velocity shear layer is an important source of Region-1 FAC at Earth. In consequence, when the

reconnection rate is high, we expect stronger FACs. At Earth, magnetopause reconnection mainly occurs for large magnetic shear across the magnetopause. In contrast to this, DiBraccio et al. (2013) showed that reconnection at Mercury occurs for any magnetic shear and Poh et al. (2016) suggested that the difference in plasma-β across the magnetopause is mainly responsible for the occurrence of reconnection. Furthermore, Scurry et al. (1994) showed that reconnection efficiency increases for low β in the solar wind at Earth. According to Slavin and Holzer (1981), at Earth we expect to have $\beta \approx 1.7$ whereas at Mercury we should assume $0.5 \leq \beta \leq 0.9$.

3.3.1. Plasma-β Estimation From TAO Model

Due to the lack of a full coverage of the magnetosheath with plasma measurements of MESSENGER, we rely on modeling to estimate the β for each orbit. Anderson et al. (1997) showed that for a perpendicular, strong shock an upper limit for the magnetosheath β is determined from the Alfvénic Mach number M_A in the solar wind:

$$\beta_{\text{sheath}} = \frac{3}{32} M_A^2 \tag{23}$$

for an adiabatic coefficient of $\gamma = 5/3$. The current M_A for each MESSENGER orbital pericenter is estimated from the TAO solar wind model. The TAO solar wind propagation model (Tao et al., 2005) provides information on the solar wind plasma velocity, density and temperature, as well as the radial and azimuthal magnetic field components, at a certain time and heliospheric distances. The simulation output is based on the OMNI solar wind 1-hr data (King & Papitashvili, 2005) of solar wind variations observed near the Earth and propagated back to Mercury's position, using a 1-dimensional magnetohydrodynamic (MHD) model. This data is then used for the classification in Figure 7.

3.3.2. Plasma-β From FIPS Instrument

The analysis of the Fast Imaging Plasma Spectrometer data (FIPS) onboard MESSENGER provides ion densities (n) and temperatures (T) for 60 s intervals. We assume that the spatial changes of plasma-β in the subsolar magnetosheath and also the electron contribution are negligible.

With

$$\beta_{\text{sheath}} = \frac{n k_{\text{B}} T}{\frac{B^2}{2\mu_0}} \tag{24}$$

we compute the plasma-β, with k_B being the Boltzmann constant. To obtain a plasma-β value for each orbit we only use data from the magnetosheath region and take the median value of all available data points per orbit to avoid distortion by outliers. FIPS mainly measured the plasma properties within a 30° cone angle. Due to the lack of coverage on the dawn and the dusk side there are no plasma-β values for terminator orbits and thus no radial current values in Figure 7.

4. Discussion

In Figure 6 the residuals of the northern hemisphere can be seen. The residuum in B_x-direction is positive close to the poles and negative on the day side between 30° and 60°. We interpret the positive deviation as indication for closure currents of the field-aligned currents. Due to Ampères law a current flowing from dawn (90°) to dusk (270°) below the orbit of MESSENGER would produce a higher B_x signature. This direction of closure currents is consistent with the FAC-analysis in Figure 7. It is not yet clear which effect causes the negative deviation on the day side in the B_x-component. One possible explanation is a cusp related magnetic depression.

We find the smallest residuum in the B_y-component (see Figure 6). Relatively strong deviations in positive and negative direction are found on the day side, which might also be cusp related. Deviations closer to equator might stem from magnetopause crossings.

Regarding the B_z-component we find the residua to be negative in general. This means that the KTH22-model underestimates this component. Note that an optimization toward yields significantly worse results in B_x.

Close to the north pole on the day side the KTH22 estimation of the magnetic field is too strong because here the effects of the cusps might play a role and are not yet included in the model.

From these magnetic field residuals the curl in spherical coordinates is taken to calculate the current in radial direction for analyzing the field-aligned currents. As explained in Section 3.2 the subdivision was made to investigate the effects of the different solar wind conditions. The top row of Figure 7 shows that the strength of the radial currents increases with a higher magnetic activity. The currents are more intense and show a larger extension toward lower latitudes. Higher magnetic activity inside the magnetosphere indicates higher reconnection rates and thus leads to stronger R1 FAC. At Earth, reconnection is mainly observed while the B_z-component of the IMF is negative. Although hybrid simulations predict a strong dependency between the FAC and the IMF shear angle at Mercury (Exner, 2021) we do not observe this.

Our hypothesis is that the flow shear in the low-latitude boundary layer at the inner edge of the magnetopause that may be formed by reconnection or viscous processes at Mercury (Anderson et al., 2011) also drives FAC (Johnson & Wing, 2015). As magnetopause reconnection appears for all magnetic shear angles for low plasma-β conditions Poh et al. (2016), we do not expect an influence of the IMF B_z-component on the FAC strength (DiBraccio et al., 2013). In agreement therewith, we do not see a clearly visible difference between the two plots (c) and (d) in the middle row associated to southward and northward IMF conditions. However, the IMF B_z-component is just an approximation instead of a synchronized measurement, so this must be taken with some caution.

Poh et al. (2016) analyzed cusp filaments around the Herman cusp regions. These are magnetic field depressions which are indicative of magnetic reconnection at the day side magnetopause. The authors also show that the occurrence rate in general is higher under low plasma-β.

From these results we could speculate that the reconnection rate is higher for low plasma-β. We assume that a higher reconnection rate leads to stronger FACs. However, examining the subplots (e) and (f) of Figure 7 this hypothesis can only be supported with caution. The radial currents under low plasma-β are slightly stronger. For low plasma-β, the values at 225° longitude are about twice as large as for high plasma-β conditions. Still, the results for the low plasma-β case look very scattered. In addition, one must take into account that the calculated radial currents are not strictly field-parallel close to the equator region. Hence, we conclude that the difference in strength and expansion in the radial currents under different plasma-β conditions is not entirely clear.

Furthermore the strongest FACs are always seen on or equatorwards of the OCB line in each plot. This is consistent with the hypothesis that flow shear in the low-latitude boundary layer is a driver of the FAC because this region is permeated by closed field lines.

5. Summary and Conclusions

Here we present a modular model to calculate the magnetic field inside the Hermean magnetosphere, the KTH22-Model. We adapted the model idea of Tsyganenko and Usmanov (1982), followed by Korth et al. (2015), improved the neutral sheet current module and added a new eastward flowing ring-shaped current, referred to as ring current module, as well. The new neutral sheet current model is numerically more costly but represents more accurately the neutral sheet current. The revision of the KTH22 Model allows for deeper investigations of the structure of Mercury's magnetosphere. Because the ring current module is included and there are now less side effects of the neutral sheet current stemming from ad-hoc approximations, we can have a closer look at further processes inside the magnetosphere such as the field aligned currents and their closure currents.

We find, that the strength of the field-aligned currents increases with higher magnetic activity. Furthermore, we can conclude that there is no upstream parameter identified which clearly controls the strength of the R1 FAC. The subdivision into orbits with positive/negative IMF-B_z component or higher/lower plasma-β does not point out any clear correlation.

The residuals show that there must be more processes occurring inside the Hermean magnetosphere, which are unmodeled so far. In the future, modules to describe the cusps and the field-aligned currents and their closure currents should be added to refine the magnetic field description.

Appendix A: Details of the KTH22 Model

A1. Details of the Parameters for the KTH22-Model

The scaling factor f for the subsolar stand-off distance R_{SS} is computed as follows:

$$f = f_a + DI \cdot f_b \tag{A1}$$

$$R_{SS} = f \cdot r_{hel}^{1/3} \tag{A2}$$

with $f_a = 2.14$ and $f_b = -0.00368$, where f_a and f_b have been determined as described in Korth et al. (2017).

A2. Harmonic Expansion of the Shielding Field

For each internal field source, the shielding fields produced by the Chapman-Ferraro currents within the magnetopause must be calculated. Inside the magnetosphere, the region is considered current-free, thus we can assume a potential ansatz:

$$\vec{B}_{cf} = -\nabla\Psi. \tag{A3}$$

For the potential Ψ we use the expansion:

$$\Psi = \sum_{i=0}^{N} a_i \exp\left(\sqrt{p_i^2 + q_i^2}\,(x - x_{shift,i})\right) \cos(p_i y) \sin(q_i z). \tag{A4}$$

The magnetic field components are

$$B_x = -\sum_{i=0}^{N} a_i \sqrt{p_i^2 + q_i^2} \exp\left(\sqrt{p_i^2 + q_i^2}\,(x - x_{shift,i})\right) \cos(p_i y) \sin(q_i z) \tag{A5}$$

$$B_y = \sum_{i=0}^{N} a_i p_i \exp\left(\sqrt{p_i^2 + q_i^2}\,(x - x_{shift,i})\right) \sin(p_i y) \sin(q_i z) \tag{A6}$$

$$B_z = -\sum_{i=0}^{N} a_i q_i \exp\left(\sqrt{p_i^2 + q_i^2}\,(x - x_{shift,i})\right) \cos(p_i y) \cos(q_i z). \tag{A7}$$

Here, we use MSM coordinates and expanded the ansatz from Korth et al. (2015) with the x_{shift} parameter.

At the magnetopause, the normal direction must be found in order to obtain the normal magnetic field. For this, two additional vectors parallel to the magnetopause are calculated. The first is found via a rotation about the symmetry axis (x-axis) at the angle $\gamma = \arctan(y/z)$. The vector components are:

$$e_x = 0 \tag{A8}$$

$$e_y = \sin\gamma \tag{A9}$$

$$e_z = \cos\gamma. \tag{A10}$$

The second vector tangential to the magnetopause is found along a small change in ϵ in the parameter description of the magnetopause described by Equation 1. Note: this change does not affect the γ-angle. The vector is then defined as

$$d\vec{r}_{mp} = \vec{r}_{mp}(\epsilon + d\epsilon) - \vec{r}_{mp}(\epsilon). \tag{A11}$$

The magnetopause normal direction is found by taking the cross-product:

$$\vec{n} = \vec{e} \times d\vec{r}_{mp}/|d\vec{r}_{mp}| \quad \text{(A12)}$$

For deriving the parameters a, p, q, and x_{shift}, we minimized B_n with a Downhill-Simplex method.

Data Availability Statement

MESSENGER MAG data were obtained from: https://pds-ppi.igpp.ucla.edu/search/view/?f=yes&id=pds://PPI/mess-mag-calibrated/data (NASA Planetary Data System, 2021). MESSENGER FIPS data were obtained from: https://pds-ppi.igpp.ucla.edu/search/view/?f=yes&id=pds://PPI/MESS-E_V_H_SW-EPPS-3-FIPS-DDR-V2.0/DATA/FIPS_NTP (Raines, 2017). The KTH22 model is available under: https://github.com/Krissy37/KTH22-model.git (Pump & Heyner, 2023). For this study we use version 8.

Acknowledgments
We thank the AMDA database for providing the solar wind plasma and magnetic field data of the TAO model on the their website (http://amda.cdpp.eu/). The TAO model is based on the Coordinated Astronomical Numerical Software (CANS), which is public available and can be retrieved on the website http://www.astro.phys.s.chiba-u.ac.jp/netlab/pub/index.html. K.P. and D.H. were supported by the German Ministerium für Wirtschaft und Klimaschutz and the German Zentrum für Luft- und Raumfahrt under contract 50QW1501 and 50QW2202. K.P. and D. H. were supported by DFG (German Research Foundation) under contract HE 8016/3-1. W.E. has been supported by DFG under contract HE8016/1-1 and by an ESA Research Fellowship. The MESSENGER mission is supported by the NASA Discovery Program, under contracts NAS5-97271 to The Johns Hopkins University Applied Physics Laboratory and NASW-00002 to the Carnegie Institution of Washington. MESSENGER MAG data were obtained from: https://pds-ppi.igpp.ucla.edu/search/view/?f=yes&id=pds://PPI/mess-mag-calibrated/data. MESSENGER FIPS data were obtained from: https://pds-ppi.igpp.ucla.edu/search/view/?f=yes&id=pds://PPI/MESS-E_V_H_SW-EPPS-3-FIPS-DDR-V2.0/DATA/FIPS_NTP. The KTH22 model is available under: https://github.com/Krissy37/KTH22-model.git. Open Access funding enabled and organized by Projekt DEAL.

References

Alexeev, I. I., Belenkaya, E. S., & Clauer, C. R., Jr. (2000). A model of region 1 field-aligned currents dependent on ionospheric conductivity and solar wind parameters. *Journal of Geophysical Research*, *105*(A9), 21119–21127. https://doi.org/10.1029/2000JA900052

Anderson, B. J., Johnson, C. L., & Korth, H. (2013). A magnetic disturbance index for Mercury's magnetic field derived from MESSENGER magnetometer data. *Geochemistry, Geophysics, Geosystems*, *14*(9), 3875–3886. https://doi.org/10.1002/ggge.20242

Anderson, B. J., Johnson, C. L., Korth, H., Slavin, J. A., Winslow, R. M., Phillips, R. J., et al. (2014). Steady-state field-aligned currents at Mercury. *Geophysical Research Letters*, *41*(21), 7444–7452. https://doi.org/10.1002/2014GL061677

Anderson, B. J., Johnson, C. L., Korth, H., Winslow, R. M., Borovsky, J. E., Purucker, M. E., et al. (2012). Low-degree structure in Mercury's planetary magnetic field. *Journal of Geophysical Research*, *117*(E12), E00L12. https://doi.org/10.1029/2012JE004159

Anderson, B. J., Phan, T.-D., & Fuselier, S. A. (1997). Relationships between plasma depletion and subsolar reconnection. *Journal of Geophysical Research*, *102*(A5), 9531–9542. https://doi.org/10.1029/97JA00173

Anderson, B. J., Slavin, J. A., Korth, H., Boardsen, S. A., Zurbuchen, T. H., Raines, J. M., et al. (2011). The dayside magnetospheric boundary layer at Mercury. *Planetary and Space Science*, *59*(15), 2037–2050. https://doi.org/10.1016/j.pss.2011.01.010

Andrews, G. B., Zurbuchen, T. H., Mauk, B. H., Malcom, H., Fisk, L. A., Gloeckler, G., et al. (2007). The energetic particle and plasma spectrometer instrument on the MESSENGER spacecraft. *Space Science Reviews*, *131*(1–4), 523–556. https://doi.org/10.1007/s11214-007-9272-5

Benkhoff, J., Casteren, J., Hayakawa, H., Fujimoto, M., Laakso, H., Novara, M., et al. (2010). BepiColombo—Comprehensive exploration of Mercury: Mission overview and science goals. *Planetary and Space Science*, *58*(1–2), 2–20. https://doi.org/10.1016/j.pss.2009.09.020

Benkhoff, J., Murakami, G., Baumjohann, W., Besse, S., Bunce, E., Casale, M., et al. (2021). BepiColombo-mission overview and science goals. *Space Science Reviews*, *217*(8), 1–56. https://doi.org/10.1007/s11214-021-00861-4

DiBraccio, G. A., Slavin, J. A., Boardsen, S. A., Anderson, B. J., Korth, H., Zurbuchen, T. H., et al. (2013). MESSENGER observations of magnetopause structure and dynamics at Mercury. *Journal of Geophysical Research: Space Physics*, *118*(3), 997–1008. https://doi.org/10.1002/jgra.50123

Exner, W. (2021). Modeling of Mercury's magnetosphere under different solar wind conditions". (Dissertation). TU Braunschweig.

Exner, W., Simon, S., Heyner, D., & Motschmann, U. (2020). Influence of Mercury's exosphere on the structure of the magnetosphere. *Journal of Geophysical Research: Space Physics*, *125*(7), e2019JA027691. https://doi.org/10.1029/2019ja027691

Genova, A., Hussmann, H., Van Hoolst, T., Heyner, D., Iess, L., Santoli, F., et al. (2021). Geodesy, geophysics and fundamental physics investigations of the BepiColombo mission. *Space Science Reviews*, *217*(2), 31. https://doi.org/10.1007/s11214-021-00808-9

Gershman, D. J., Dorelli, J. C., DiBraccio, G. A., Raines, J. M., Slavin, J. A., Poh, G., & Zurbuchen, T. H. (2016). Ion-scale structure in Mercury's magnetopause reconnection diffusion region. *Geophysical Research Letters*, *43*(12), 5935–5942. https://doi.org/10.1002/2016GL069163

Glassmeier, K.-H., Auster, H.-U., Heyner, D., Okrafka, K., Carr, C., Berghofer, G., et al. (2010). The fluxgate magnetometer of the BepiColombo Mercury planetary orbiter. *Planetary and Space Science*, *58*(1), 287–299. (Comprehensive Science Investigations of Mercury: The scientific goals of the joint ESA/JAXA mission BepiColombo). https://doi.org/10.1016/j.pss.2008.06.018

Heyner, D., Auster, H.-U., Fornaçon, K.-H., Carr, C., Richter, I., Mieth, J. Z. D., et al. (2021). The BepiColombo planetary magnetometer MPO-MAG: What can we learn from the Hermean magnetic field? *Space Science Reviews*, *217*(4), 52. https://doi.org/10.1007/s11214-021-00822-x

James, M. K., Imber, S. M., Bunce, E. J., Yeoman, T. K., Lockwood, M., Owens, M. J., & Slavin, J. A. (2017). Interplanetary magnetic field properties and variability near Mercury's orbit. *Journal of Geophysical Research: Space Physics*, *122*(8), 7907–7924. https://doi.org/10.1002/2017JA024435

Johnson, J. R., & Wing, S. (2015). The dependence of the strength and thickness of field-aligned currents on solar wind and ionospheric parameters. *Journal of Geophysical Research: Space Physics*, *120*(5), 3987–4008. https://doi.org/10.1002/2014JA020312

King, J. H., & Papitashvili, N. E. (2005). Solar wind spatial scales in and comparisons of hourly wind and ace plasma and magnetic field data. *Journal of Geophysical Research*, *110*(A2), A02104. https://doi.org/10.1029/2004JA010649

Korth, H., Johnson, C. L., Philpott, L., Tsyganenko, N. A., & Anderson, B. J. (2017). A dynamic model of Mercury's magnetospheric magnetic field. *Geophysical Research Letters*, *44*(20), 10147–10154. https://doi.org/10.1002/2017GL074699

Korth, H., Tsyganenko, N. A., Johnson, C. L., Philpott, L. C., Anderson, B. J., Al Asad, M. M., et al. (2015). Modular model for Mercury's magnetospheric magnetic field confined within the average observed magnetopause. *Journal of Geophysical Research: Space Physics*, *120*(6), 4503–4518. https://doi.org/10.1002/2015JA021022

Milillo, A., Fujimoto, M., Murakami, G., Benkhoff, J., Zender, J., Aizawa, S., et al. (2020). Investigating Mercury's environment with the two-spacecraft BepiColombo mission. *Space Science Reviews*, *216*(5), 93. https://doi.org/10.1007/s11214-020-00712-8

NASA Planetary Data System. (2021). MESSENGER MAG calibrated data bundle [Dataset]. https://doi.org/10.17189/1522383

Nelder, J. A., & Mead, R. (1965). A simplex method for function minimization. *The Computer Journal*, *7*(4), 308–313. https://doi.org/10.1093/comjnl/7.4.308

Poh, G., Slavin, J. A., Jia, X., DiBraccio, G. A., Raines, J. M., Imber, S. M., et al. (2016). Messenger observations of cusp plasma filaments at Mercury. *Journal of Geophysical Research: Space Physics*, *121*(9), 8260–8285. https://doi.org/10.1002/2016JA022552

Pump, K., & Heyner, D. (2023). KTH22 model [Software]. https://zenodo.org/record/8319407
Raines (2017). MESSENGER EPPS FIPS derived data archive [Dataset]. https://doi.org/10.17189/1519743
Rong, Z. J., Ding, Y., Slavin, J. A., Zhong, J., Poh, G., Sun, W. J., et al. (2018). The magnetic field structure of Mercury's magnetotail. *Journal of Geophysical Research: Space Physics*, *123*(1), 548–566. https://doi.org/10.1002/2017JA024923
Scurry, L., Russell, C. T., & Gosling, J. T. (1994). Geomagnetic activity and the beta dependence of the dayside reconnection rate. *Journal of Geophysical Research*, *99*(A8), 14811–14814. https://doi.org/10.1029/94JA00794
Shi, Z., Rong, Z. J., Fatemi, S., Slavin, J. A., Klinger, L., Dong, C., et al. (2022). An eastward current encircling Mercury. *Geophysical Research Letters*, *49*(10), e2022GL098415. https://doi.org/10.1029/2022GL098415
Shue, J. H., Chao, J. K., Fu, H. C., Russell, C. T., Song, P., Khurana, K. K., & Singer, H. J. (1997). A new functional form to study the solar wind control of the magnetopause size and shape. *Journal of Geophysical Research*, *102*(A5), 9497–9512. https://doi.org/10.1029/97JA00196
Slavin, J. A., Anderson, B. J., Baker, D. N., Benna, M., Boardsen, S. A., Gloeckler, G., et al. (2010). Messenger observations of extreme loading and unloading of Mercury's magnetic tail. *Science*, *329*(5992), 665–668. https://doi.org/10.1126/science.1188067
Slavin, J. A., & Holzer, R. E. (1981). Solar wind flow about the terrestrial planets 1. Modeling bow shock position and shape. *Journal of Geophysical Research*, *86*(A13), 11401–11418. https://doi.org/10.1029/JA086iA13p11401
Sun, W. J., Fu, S. Y., Slavin, J. A., Raines, J. M., Zong, Q. G., Poh, G. K., & Zurbuchen, T. H. (2016). Spatial distribution of Mercury's flux ropes and reconnection fronts: Messenger observations. *Journal of Geophysical Research: Space Physics*, *121*(8), 7590–7607. https://doi.org/10.1002/2016JA022787
Tao, C., Kataoka, R., Fukunishi, H., Takahashi, Y., & Yokoyama, T. (2005). Magnetic field variations in the Jovian magnetotail induced by solar wind dynamic pressure enhancements. *Journal of Geophysical Research*, *110*(A11), A11208. https://doi.org/10.1029/2004JA010959
Tsyganenko, N., & Usmanov, A. (1982). Determination of the magnetospheric current system parameters and development of experimental geomagnetic field models based on data from IMP and HEOS satellites. *Planetary and Space Science*, *30*(10), 985–998. https://doi.org/10.1016/0032-0633(82)90148-9
Tsyganenko, N. A. (1995). Modeling the Earth's magnetospheric magnetic field confined within a realistic magnetopause. *Journal of Geophysical Research*, *100*(A4), 5599–5612. https://doi.org/10.1029/94JA03193
Wang, J., Huo, Z., & Zhang, L. (2022). Reconstructing Mercury's magnetic field in magnetosphere using radial basis functions. *Planetary and Space Science*, *210*, 105379. https://doi.org/10.1016/j.pss.2021.105379
Wardinski, I., Amit, H., Langlais, B., & Thébault, E. (2021). The internal structure of Mercury's core inferred from magnetic observations. *Journal of Geophysical Research: Planets*, *126*(12), 0–31. https://doi.org/10.1029/2020je006792
Winslow, R. M., Anderson, B. J., Johnson, C. L., Slavin, J. A., Korth, H., Purucker, M. E., et al. (2013). Mercury's magnetopause and bow shock from MESSENGER Magnetometer observations. *Journal of Geophysical Research: Space Physics*, *118*(5), 2213–2227. https://doi.org/10.1002/jgra.50237
Zhao, J.-T., Zong, Q.-G., Yue, C., Sun, W.-J., Zhang, H., Zhou, X.-Z., et al. (2022). Observational evidence of ring current in the magnetosphere of Mercury. *Nature Communications*, *13*(1), 924. https://doi.org/10.1038/s41467-022-28521-3